DOI: 10.13009/EUCASS2019-1038

8TH EUROPEAN CONFERENCE FOR AERONAUTICS AND AEROSPACE SCIENCES (EUCASS)

DOI: ADD DOINUMBER HERE

Deployment of CubeSats From Low-Earth Orbit to Near-Earth Asteroids

Sintia Jaworski[⋆†] *and Jan Kindracki*[⋆]
[⋆]*Warsaw University of Technology, Faculty of Power and Aeronautics*
Nowowiejska 25, Warsaw, 01-111, Poland
sjaworski@itc.pw.edu.pl · jkind@itc.pw.edu.pl
[†]Corresponding author

Abstract

The present study investigates the synchronized deployment of 6U cubeSats from low-Earth orbit to near-Earth asteroids. It was found that for an escape time of 300 days, solar cell and battery degradation are 11% and 28%, respectively, where an orbital plane inclination of 51.6° reduces the overall radiation dosage. Suboptimal interplanetary trajectories were obtained using differential evolution, with a ΔV maneuver used to relate the Earth and interplanetary phases. Individual mission ΔV's fall between 1 - 2.5 km/s, where the low thrust propellant required is between 2.76 and 3.46 kg.

1. Introduction

CubeSats are a class of miniature satellites which have provided a platform for conducting lower cost missions in the recent past. Their design has allowed universities to conduct independent space research, without the need to send expensive larger class spacecraft and many of their components may be purchased off-the shelf which makes their production time more rapid. In addition to this, deploying from low-Earth orbit (LEO) allows a larger trajectory design space compared to piggyback missions in to regions between the Moon and Earth's sphere of influence (SOI). For instance the recent Space Launch Systems (SLS) technology created by NASA,[5] has promised the capacity to transport large payloads including manned missions to Mars in the near future. In the case of cubeSats, while such launch vehicles can signifcantly reduce Earth escape times, they can greatly increase mission costs and reduce the number of potential asteroid target candidates due to restricted launch windows and trajectory speeds.To date all cubeSat missions have been confined to LEO, with the exception of the Marco cubeSats, recently launched onboard the Mars Insight spacecraft.[18] NASA has proposed a cubeSat mission to a near-Earth asteroid (NEA) scheduled to launch in 2020,[23] which would be only the second interplanetary mission conducted by a cubeSat. The European Space Agency (ESA), has also planned for a 12U cubeSat mission to a near-Earth asteroid starting from Lagrange point, L2.[28] CubeSats pose several mission design challenges, primarily due to their small size which presents a highly constrainted optimization problem. Currently cubeSat technology is rapidly progressing, with several propulsion systems designed specifically for cubeSats in the last 10 years. Due to the rapidly evolving technology, the majority of cubeSat missions have been technology demonstration class missions. For cubeSats to extend mission capabilities beyond Earth orbits, propulsion technology must gain flight heritage to prove the capability of interplanetary cubeSat missions. Their has been a growing interest recently in near-Earth asteroid science class missions. Studying asteroid materials both visually and through lab analysis, can provide insight into questions regarding the formation of our universe. In addition to scientific observation missions, asteroid deflection missions are becoming more ambitious in hopes of preventing interplantary collisions. The most recent example of a successful asteroid mission, was that of Hayabusa 2,[10] which successfully obtained a sample from the surface of asteroid Ryugu in April of 2019.

The goal of the present work is to design a mission profile for a set of 6U cubeSats deployed from the International Space Station (ISS) to near-Earth asteroids. The contribution of this work is the feasbility assessment of whether 6U cubeSats are able to escape Earth's orbit and continue towards a near-Earth asteroid carrying on board at least one piece of scientific hardware. The economic benefits of deploying from the ISS are clear, and this work aims to address the challenges and constraints such a deployment strategy would introduce. The Japanese Aerospace Exploration Agency (JAXA) has built the JAM deployer,[9] which has the ability to deploy masses of cubeSats up to 6U. This work will lay the platform for an integrated trajectory design consisting of patching both the Earth escape and interplanetary trajectories, working towards designing cubeSat missions with increased scientific return capabilties in the future. In addition to

DOI: 10.13009/EUCASS2019-1038

the above, this work will present a deployment sequence to speed up the scientific return by sending the cubeSats on nearly parallel missions to distinct targets. CubeSats have been suggested to have the potential of generating a scientific return,[11] however propulsion technology still limits the trajectory capabilities for these small satellites. The work in[22] has demonstrated the escape of a single 3U cubeSat using constant thrusting and thrust at perigee maneuvers, indicating the potential of stand-alone cubeSat missions. The present work present results for cubeSat propulsion systems created by JPL and Tethers Unlimited, the second of which is approaching or has approached a TRL level of 6.
The algorithms and trajectory design methods demonstrated here, wihle presented for cubeSats, may extend to any class of spacecraft, however the concept of synchronizing the deployment of multiple spacecraft is particularly beneficial to scientific-class miniature satellites. The primary contributions of this work are the synchronized deployment concept for cubeSats from LEO, the systems analysis of 6U cubeSats escaping Earth and the trajectory design of ISS deployed cubeSats.

2. Methodology

The present work investigates the concept of deploying cubeSats from the ISS, bound on nearly parallel missions from LEO to near-Earth asteroids. As a result the combined trajectories, cubeSat mass and propellant requirements are more constrained than in typical mission/trajectory design, as will be demonstrated. In the first stage of trajectory design, each cubeSat will escape Earth using the modelling presented in Section 3. The start of each cubeSat begins from the ISS, where the initial state of the cubeSat at the start of the escape maneuver is assumed to be that of the ISS. In present reality such a deployment would take place using the ISS deployer,[9] which does create a small relative velocity between the cubeSat and ISS, however this will be taken as negligable in the present work. As will be presented in Section 4.1, the date of deployment will effect the ISS orbital state. In this work the global optimization method for interplanetary trajectories requires that the epoch date for the i^{th} cubeSat, $\tilde{t}_{0,i}$, remain an open parameter of the optimization. This then implies, that the epoch for cubeSat deployment from LEO is, $t_{0,i} = \tilde{t}_{0,i} - t_{esc}$, where t_{esc} is the time of flight for the Earth escape maneuver, which is considered to be fixed for all cubeSats. The time of escape is predicted using a systems analysis of escape conditions. Studies revealed that varying the Earth escape trajectory epoch, $t_{0,i}$ did not significantly impact the escape parameters and profiles, and so a nominal date of May 15, 2019, was used to predict the eclipse behaviour and compute t_{esc}. The escape maneuver produces a fixed SOI velocity, which places constraints on the initial velocity of the interplanetary trajectory in order to obtain a reasonable sampling of feasible trajectories. This is discussed in Section 4. It should be noted that in this work V_∞ is taken to be the velocity at the SOI in the inertial frame of the escaping body, in this case, Earth. This is not to be confused with the hyperbolic excess velocity for ballistic trajectories. The result of patching the trajectories through the hyperbolic escape velocity results in a required ΔV_{corr} maneuver, necessary to re-orientate the spacecraft to the optimized interplanetary trajectory. Due to the variation of the ISS orbital state, the deployment conditions must be predicted, to try and accurately compute the propellant required for the ΔV_{corr} maneuver. The variation of the ISS conditions are discussed in Section IV.4.1, however to present the preliminary concept of the propsed mission, the ISS orbital state is fixed to what is reported on the reference date of May 15, 2019. This allows a ranking of the propellant required for the entire mission for each cubeSat, which will produce a distinct sequence of targets and deployment dates to demonstrate the trajectory design method and target selection algorithm. Solutions will be proposed for how to deal with varying ISS parameters in Section 5. The escape maneuver is the primary way to assert the feasbility of such a mission for a cubeSat. Due to the mass and volume constraints of cubeSats, a full systems analysis is performed during escape to ensure that their is sufficient solar power, battery power and propellant remaining for the interplanetary trajectory. These results are presented in Sections 3.1, 3.2 and 3.3. To synchronize the deployment of n cubeSats, two objectives of the mission are fulfilled in sequence. The first objective will aim to reduce the propellant primarily through global optimization of the interplanetary trajectory, the second objective tries to parallelize the individual cubeSat missions after the final set of candidates is selected based on the criteria outline in Section 4.1.

3. Earth Escape

To model the escape, the modified equinoctial (ME) equations of motion are used with thrust in the direction of the velocity vector. Thrusting in the direction of velocity provides an instantaneous two-body energy increase. This form of the equations was selected to avoid singularities for circular orbits and to capture the changing orbit conditions between circular to elliptical states. The ME equations were also selected due to no restriction of a constant mass flux,

DOI: 10.13009/EUCASS2019-1038

which is required for the polar equations for orbit raising.[26] The ME orbit equations may be written as,

$$\dot{p} = \frac{2p}{w}\sqrt{\frac{p}{\mu}}a_\theta \tag{1}$$

$$\dot{f} = \sqrt{\frac{p}{\mu}}\Big(a_r\sin(L) + [(w+1)\cos(L) + f]\frac{a_\theta}{w} - [h\sin(L) - k\cos(L)]\frac{ga_n}{w}\Big) \tag{2}$$

$$\dot{g} = \sqrt{\frac{p}{\mu}}\Big(-a_r\cos(L) + [(w+1)\sin(L) + g]\frac{a_\theta}{w} + [h\sin(L) - k\cos(L)]\frac{ga_n}{w}\Big) \tag{3}$$

$$\dot{h} = \sqrt{\frac{p}{\mu}}\frac{s^2 a_n}{2w}\cos(L) \tag{4}$$

$$\dot{k} = \sqrt{\frac{p}{\mu}}\frac{s^2 a_n}{2w}\sin(L) \tag{5}$$

$$\dot{L} = \sqrt{\mu p}\left(\frac{w}{p}\right)^2 + \frac{1}{w}\sqrt{\frac{p}{\mu}}\Big(h\sin(L) - k\cos(L)\Big)a_n \quad , \tag{6}$$

where p, f, g, h, k, L are the modified elements related to the Keplerian orbital elements though well-known relations[26].[2] The thrust acceleration vector, $\mathbf{a} = [a_r, a_\theta, a_n]$ is then computed as,

$$\mathbf{a} = \frac{T}{m}\mathbf{Q}^T\frac{\vec{\mathbf{V}}_{ECI}}{\|\vec{\mathbf{V}}_{ECI}\|} \quad , \tag{7}$$

where $\mathbf{Q}$ is the transformation matrix between the frame of reference in the ME equations (normal, radial and tangential) frame and the Earth centered intertial (ECI) frame of reference and $\vec{\mathbf{V}}_{ECI}$, is the spacecraft velocity in the ECI frame. The escape profiles for the velocity and eccentricity versus orbital altitude are shown in Figures 1(a)-1(b). The initial velocity of the spacecraft at deployment is roughly 7.6 km/s, achieving an SOI velocity, V_∞, of 0.895 km/s, corresponding to a C3 of $\sim 0.8\ km^2/s^2$. Since the escape trajectory is not ballistic the final eccentricity is roughly 0.9, corresponding to elliptic orbit conditions rather than hyperbolic. The presence of a thrust force, particulary where the gravity field is weak near the SOI, allows the spacecraft to escape under non-hyperbolic conditions. Figures 1(c)-1(d) show the eclipse behaviour experienced by the spacecraft, where the ME equations are integrated using RK4 until the spacecraft orbital radius, r, no longer satisfies the condition $r < 925000$. In particular the β-angle lies within a subset of the range of β angles experienced by the ISS throughout a full year and full range of its longitude of ascending node, Ω. Presently, the spacecraft only experiences a subset of this range, [-75, 75]°, due to the fact that the Ω of the spacecraft orbital state remains fixed throughout the escape maneuver. Only the variation of the Sun's revolution around the Earth during the period of escape of 300 days contributes to the demonstrated variation in β. The eclipse profile reveals two locations of eclipse at altitudes of roughly 4000 km and 30,000 km. In Figure 1(d), the switch function refers to a {0,1} valued function where 0 indicates no eclipse is occuring and 1 indicates an eclipse is occuring. The second eclipse region experience significantly shorter eclipse fractions, θ_{ecl}, than the first, however its eclipse durations are longer due to greater orbital periods at higher altitudes. Figure 2 demonstrates the escape orbit raising profile in $\mathbb{R}^3$ space, where the inclination of the orbital plane remains fixed at 51.6°, which corresponds to the ISS orbital inclination at time of deployment.

3.1 Radiation Model

To accurately model the effects of radiation in the Van Allen radiation belts, the AE9/AP9 models[20] were implemented. The threshold energies for electron and protons were taken at levels of 1MeV and 10 MeV, respectively. The accumulated fluences are computed according to,

$$\mathcal{F}_{p,e} = \sum_{i=1}^{R^*}\Big(\int_{\tau_i} J_{E_\geq} dt\Big) \quad , \tag{8}$$

where R^* denote the set of all revolutions, whose initial altitudes remain below 60,000 km, $J_{E_\geq}$ is the omni-directional flux[1] for threshold energy, E and τ_i is the time period of the i^{th} revolution. The initial solar panel capacity is sized based on what is reported for commerical 6U buses, which for Blue Canyon is reported at 118W.[3] In this work the initial panel capacity is set to a slightly higher level of 125W, which could reflect more advanced solar technology in the near future. Figure 3, shows the altitude versus time of flight for the escape maneuver, where the time spent in the radiation belts has been computed at 225 days. While this is sufficiently long, and radiation damage is a concern, particularly for a cubeSat, due to the orbital plane inclination of 51.6 °, the solar cell degradation is significantly less than what would

DOI: 10.13009/EUCASS2019-1038

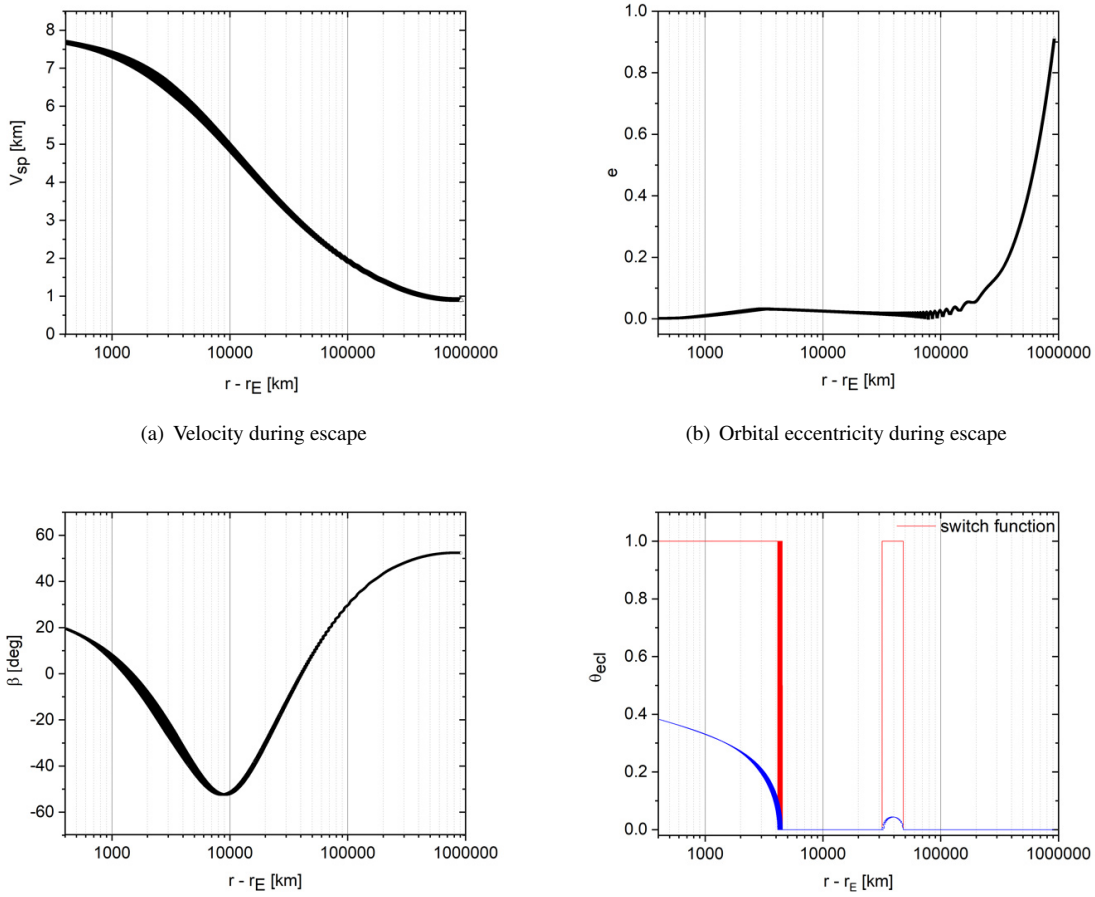

(a) Velocity during escape

(b) Orbital eccentricity during escape

(c) β-angle during escape

(d) Eclipse profile

Figure 1: Escape profiles

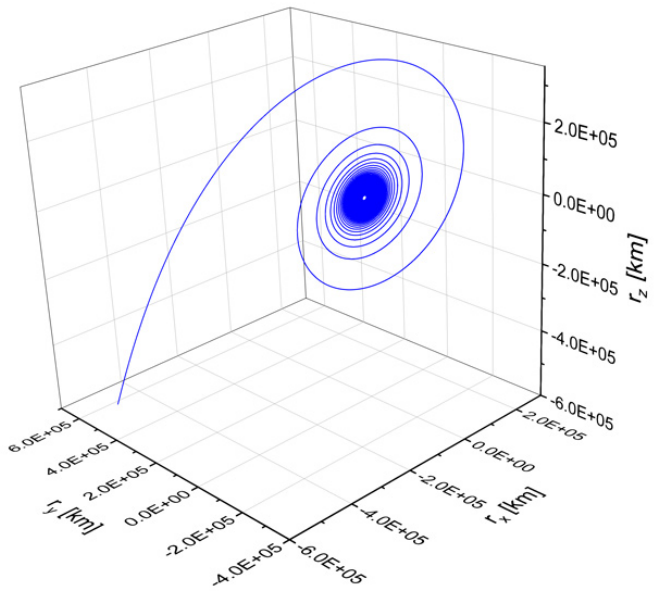

Figure 2: Escape trajectory in $\mathbb{R}^3$

DOI: 10.13009/EUCASS2019-1038

be experienced for an equatorial orbit. Figure 4(a) demonstrates the solar cell degradation, where damage for a given fluence due to protons and electrons has been obtained from extracted plot data in.[15]

3.2 Battery Model and Eclipse Analysis

The battery sizing in this work is sized from the storage capacity provided by the Blue Canyon XB6 Bus. This is reported as having an initial storage capacity between 75-185 Whr,[3] with a voltage range between 9-23 V. $LiFePO_4$ cells are commonly used for spacecraft missions and have a long flight heritage[17] and so battery degradation models of $LiFePO_4$ cells were selected. The storage capacity of a commercial 6U cubeSat bus indicates that 21 cells can be arranged to produce a battery with storage capactity of 172 Whr at a voltage of 23V. To model the degradation of the battery, the following model was implemented,[29]

$$Q_{loss} = a\mathrm{e}^{(-\mathrm{b}/(8.314\mathrm{T}))}\mathrm{A_h}^{\mathrm{c}} \quad , \tag{9}$$

where parameters a, b, c are selected and fitted based on the battery C-rate, which was selected as 1C in the present work. This produced parameter values of 25000, 31300 and 0.553, respectively. The variable, Ah is defined as $\mathrm{A_h} = \mathrm{C_{batt}} * \mathrm{DOD} * \mathrm{n_{cyc}}$, where C_{batt} is the cell capacity in [Ah], DOD is the degree of discharge and n_{cyc} is the battery cycle number. Q_{loss} is the percentage of initial cell capacity lost. For $LiFePO_4$ the cell capacity is 2.5 Ah with a nominal voltage of 3.3 V. The method of selecting the power level for thrusting during eclipse, allows for DOD values below 1, which increases the battery capacity at the start of the interplanetary mission. During the esape period of 300 days, a total of 100 battery cycles contributed to the battery degradation. Figure 4(b) shows the final battery storage capacity at the end of the escape maneuver, which dropped from an initial value of 173 Whr to 125 Whr, which should remain sufficient for the interplanetary trajectory, which does not experience eclipse regions. The battery degradation is primarily effected by the eclipse behaviour during escape, which occurs twice over the period of 300 days. Cylindrical shadow analysis is used to assess whether or not eclipse will occur, indicated by the *switch function* in Figure 1(d). For circular orbits an eclipse occurs at orbital radii defined by,[8]

$$r < \frac{r_E}{sin(|\beta|)} \quad , \tag{10}$$

where r_E is the Earth's radius and β is the Sun β-angle shown in Figure 1(c). Eqn. (10) is simply the switch function. It's noted that a circular shadow analysis was relevant for the altitudes where en eclipse is experienced, as demonstrated by Figures 1(b) and 1(d). In addition to computing eclipse duration, the eclipse entry and exit angle were also computed so the thrust level could be reduced at accurate orbital positions. The entry and exit angles are computed in reference to the i^{th}'s orbit true anamoly,[19]

$$p^2 = r_E^2 + p^2(b_1\cos(\nu) + \mathrm{b_2}\sin^2(\nu)) \quad , \tag{11}$$

where $p = a(1-e^2)$, is the semi latus rectum as functions of semi-major axis and eccentricity and ν is the true anomly to be computed. The numerical method used in this work obtains one root for Eqn. (11), which corresponds to either the entry or exit angle. Analyzing the derivative of the above equation can deduce which angle is computed and the other angle is obtained through knowledge of the eclipse transition angle, $\Delta\theta$. Parameters, b_1, b_2 are function of the orbital state parameters, and details can be found in.[19] It may be noted that an appropriate transformation between absolute transition angle and orbit true anomaly are applied. The absolute transition angle refers to the angle transitioned during a revolution relative to the starting position in $\mathbb{R}^3$ at time of deployment.

3.3 Power

To assess the feasibility of the escape trajectory, power constraints were implemented. The analysis performed in this work takes into consideration both solar panel and battery degradation. The solar cell degradation results from the time spent in the Van Allen radiation belts, presently assumed to fall between altitudes of 400 to 60,000 km. The power constraints are addressed through conservation of energy at each point of analysis. The thrust level is set at a level which addresses the following constraints,

$$P_{solar}t_{sun} \leq (P_{th,sun} + P_{nom})t_{sun} + P_{th,ecl}t_{ecl} \tag{12}$$

and for the batteries during period with eclipse,

$$P_{th,ecl}t_{ecl} \leq E_{batt} \quad , \tag{13}$$

where $P_{solar}, P_{th,ecl}, P_{th,sun}t_{sun}, t_{ecl}, E_{batt}$ are the power provided by the solar panels, the power level for thrusting in a region of eclipse, the power level for thrusting in the Sun, the duration of time spent in the Sun, the duration of time

DOI: 10.13009/EUCASS2019-1038

spent in an eclipse and the energy stored in the battery. The power required for nominal operations, P_{nom}, are assumed fixed througout the escape maneuver, and set to a value of 6 W. In addition to the inequalities in Eqns. (12) and (13), the power levels must obey the performance bounds of the selected thruster,

$$P_{min} \geq P_{th,sun} \leq P_{max} \ , \tag{14}$$

$$P_{min} \geq P_{th,ecl} \leq P_{max} \ . \tag{15}$$

The power analysis is performed at the end of each complete orbital revolution. Particle fluences are integrated over the duration of a revolution, which was discussed in Section 3.1, where solar cell degradation is applied prior to the start of a new revolution. At the beginning of each revolution or orbit, the thrust levels are set according to two different scenarios. The first scenario is one where an orbit experiences an eclipse. Here the thrust magnitude is calculated based on a series of conditionals. First the maximum thrust level (dictated by the selected thruster), is set during the time the spacecraft is in the Sun, $P^i_{th,sun} = P_{max}$. Here i denotes the i^{th} revolution, where $i \in R$, with R being the set of all revolutions. Assuming all the remaining power in the Sun is used to recharge the batteries, this yields a power thrust level during eclipse. Depending on the fraction, θ_{ecl} and duration of eclipse, t_{ecl}, this may or may not be possible due to limited battery capacity or thrust levels in the eclipse region that fall out of the achievable thrust range. In the first case, $P^i_{th,ecl} < P_{min}$, where P_{min} is the lowest power throttle level of the thruster and $P^i_{th,ecl}$ is the power level for the thrusters in the eclipse region. In this case the the thrust level in the eclipse region is reset to $P^i_{th,ecl} = P_{min}$, and the thrust level in the Sun is calculated as,

$$P^i_{th,sun} = \frac{P^i_{solar} t_{sun} - P_{min} t_{ecl} - P_{nom} t_{sun}}{t_{sun}} \ . \tag{16}$$

In this case it follows that $P^i_{th,sun} < P_{max}$. The above formulation assumes that each revolution experiences sufficient time in the Sun to allow for charging the batteries. For the selected $LiFePO_4$ cells modeled in this work, its estimated that the the time spent in the Sun for all revolutions is sufficient to recharge the batteries, where the minimum time a recharge must occur is within 52 minutes. In the next case, $P^i_{th,ecl} > P_{max}$. This means that thrusting maximum in the Sun results in a thrust level in the eclipse region that exceeds the maximum power throttle level of the thruster when all remaining solar panel power in the Sun is used to charge the battery. Here, the power level for thrust in the eclipse is reset to $P^i_{th,ecl} = P_{max}$, which allows for energy storage in the Sun, $E^i_{stored} > 0$. In the third case, the power level for the thrust in the eclipse region, exceeds the energy in the batteries. In this case, the eclipse thrust power level is reset, $P^i_{th,ecl} = E^i_{batt}/t_{ecl}$, and here $E^i_{stored} > 0$. In the last case, there are no constraint violations during eclipse when the thrust power level in the Sun is set to P_{max}. However in this case, $E^i_{stored} = 0$. Due to the long time required to escape for small satellites, it is more important to thrust at maximum level whenever possible, than to store energy, and so this condition is used as the optimal condition. During revolutions where no eclipse is experienced, the power level required for thrusting is set to $P^i_{th,sun} = P^i_{solar} - P_{nom}$. Studies revealed that reducing thrust only during eclipse periods (if possibe) still allowed the cubeSat to escape Earth in under 1 year. Alternatively, reducing the thrust level to $P_{th,ecl}$ for the entire revolution, for revolutions experiencing eclipsing, results in an Earth escape time of > 400 days. To analyze how the power constraints are satisfied, the individual revolutions are approximated by the orbital state parameters at the beginning of the revolution in regions where there is little change in e and w over the period of revolution. This is necessary to assume for altitudes where eclipse is experienced, since a cylindrical shadow analysis is performed for equivalent Keplerian orbits.[19] In regions where the orbit becomes non-circular, $e > 0.03$, eclipse is no longer experienced and the radiation and energy analysis is performed for time periods equivlent to the time of revolution. Figure 4(c) shows the energy stored versus revolution. It can be observed that in the first region with an eclipse (eclipse 1), $400 < r - r_E < 4000$, the power stored is decreasing with increasing altitude. This happens since power is stored in cases with reduced thrusting, however the eclipse fraction is decreasing and so during a revolution the period of higher thrusting is increasing, resulting in less power stored. In the second eclipse region (eclipse 2), between altitudes 30,000 to 50,000 km, corresponding to revolution point of $\sim$ 1344, stored power drops and increases in a short time period since an eclipse causes power to be stored once again, however the decreasing eclipse fraction reduces stored power as altitude increases. At the highest altitudes, where eclipse is no longer experienced, stored energy increases rapidly due to a rapid increase in the time of revolution. Figure 4(d) shown the escape orbit raising profile at the first eclipse point with coloured regions corresponding to areas where thrusting has been reduced below maximum throttle capacity.

3.4 Propulsion

The propulsion system is modeled using the performance characteristics of the MiXi Xenon thruster by NASA Jet Propulsion Labratory.[12] Previous works have demonstrated the feasbility of this thruster for 3U form factors.[4] Its performance characteristics, light weight (200 g) and smaller 3 cm diameter make it a good selection for a 6U cubeSat thruster. The MiXi thruster operates in a power range of [14, 52] W, a thrust range of [0.4, 1.5] mN, and a specific

DOI: 10.13009/EUCASS2019-1038

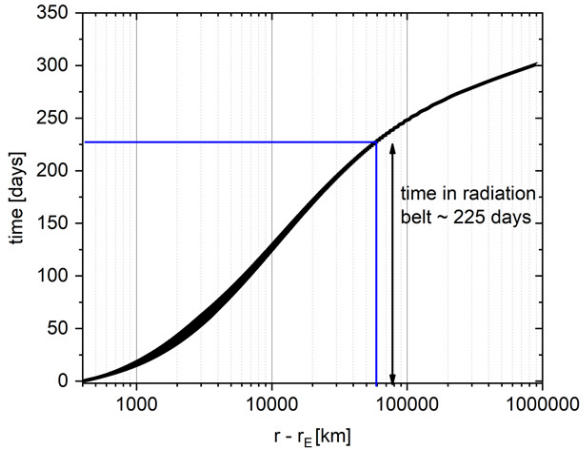

Figure 3: Time in radiation zone.

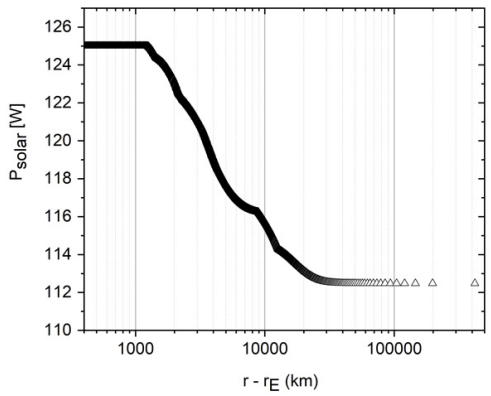

(a) Solar cell degradation

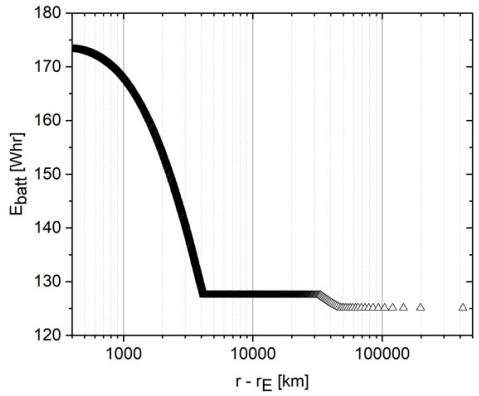

(b) Battery degradation

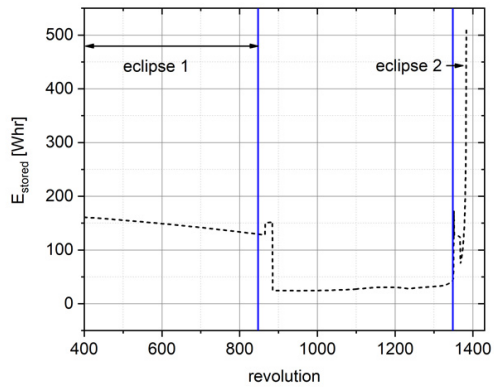

(c) Power stored

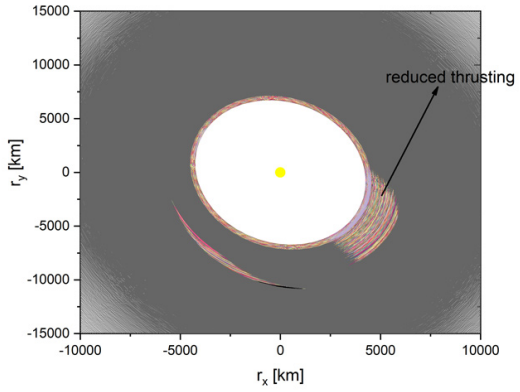

(d) Reduced thrust regions during eclipse along trajectory in $\mathbb{R}^2$

Figure 4: Power modelling during escape

impulse, I_{sp} range between [1760, 3100] s.[12] Simulations revealed the present cubeSat escape trajectory can only be achieved in reasonable time (< 1 year) using a minimum of two thrusters. Section 3.3 presented the method to select power levels for thrust within the operational range of the MiXi thruster. A linear relationship between power and

DOI: 10.13009/EUCASS2019-1038

thrust was assumed, allowing values to be obtained for the power to thrust ratio, P/T. Using the value for P/T, the I_{sp} was computed using,

$$I_{sp} = \frac{2\eta P}{gT} \quad , \tag{17}$$

where η is the total thruster efficiency set to a value of 0.45, which has been reported for ion thrusters.[4] The mass flux is then modeled according to,

$$\dot{m} = \frac{n_{th} T}{g_0 I_{sp}} \ , \tag{18}$$

where g_0 is the standard gravitational acceleration at Earth's surface and n_{th} is the number of thrusters, presently set to 2. As discussed in Section 3.3, the thrust level is varied, corresponding to non-constant values for $\dot{m}$ during escape. While the present mission architecture increases ecomonic benefits, deploying from the ISS poses limitations in trajectory design. Assuming the initial conditions at deployment coincide with the orbital state of the ISS, this restricts the direction and magnitude of the SOI velocity, $\vec{V}_\infty$, as discussed in Section 2. To overcome this issue only the direction of $\vec{V}_\infty$ remained an open parameter in the global/local optimization, where the magitude was preserved across the SOI boundary. This produces many feasible, low-propellant trajectories, however a corrective ΔV maneuver is required at the time of escape to redirect the spacecraft on the correct interplanetary trajectory. Tests revealed that cold gas, while operationally simple, cannot perform the required ΔV maneuvers using reasonable propellant masses. To minimize the total required propellant, the Hydros thruster by Tethers Inc.[12] is modelled for the required maneuver, with a specific impulse of 258 s and thrust of 0.25 N. While the thruster does add complexity to the cubeSat architecture, it is one of the simpler bi-propellant thruster designs requiring a single propellant tank for the water.[12] To this date cubeSats have been primarily constrainted to LEO, where the present work designs a mission for cubeSats whose mission goals are more ambitious, thus requiring a more complex design to achieve it's scientific objectives. The mass and volume of the Hydros thruster fall within the 6U cubeSat limits for all the proposed satellite components discussed in Section 5. The ΔV required for the orbital correction is computed as,

$$\Delta V_{corr} = \sqrt{2V_\infty^2(1 - cos(\phi)} \ , \tag{19}$$

where ϕ is the angle between $\vec{V}_\infty$ in the ECI frame and $\vec{V}_\infty$ computed from the global optimization. From Eqn. (19), the propellant required by the Hydros thruster may be computed using the rocket equation. During the low-thrust interplanetary trajectory the thrust levels are varied using throttle levels in the range [0,1] (Section 4), while fixing the I_{sp} to the maximum level. This was deemed sufficient to model the propulsion during the interplanetary phase due to reduced perturbations, reduced radiation dosages and no periods of eclipse. Varying the I_{sp} during the interplanetary phase may increase the propellant consumption from what is reported in Section 5, however the trajectories produced during this phase are predominantly coasting trajectories and so reducing I_{sp} will not likely produce significant differences.

4. Differential Evolution and Transcription

The method selected for global optimization of the interplanetary trajectory was differential evolution (DE), in combination with a local optimization process used to refine globally optimized solutions. DE's were first proposed by Storn and Price,[24] and have since been shown as effective tools for global optimization. Genetic algorithms have been explored as a successful method to obtain approximate, optimized interplanetary trajectories[27].[30] In the work of,[27] a genetic algorithm was formulated as a hybrid problem with local optimization, to obtain optimized interplanetary trajectories to Mars and Jupiter. The present work follows more closely the technique proposed by,[30] where differential evolution and local optimization are performed sequentially to refine global solutions. One reason DE was selected in the present work, was to avoid the conversion of binary strings to integers in the search space. The benefits of differential evolution algorithms is their ability to explore vast regions of the search space and their compatibility with and nonlinear and non-differentiable continuous spaces. Their limitations include that they are typically computationally expensive and they lack the mathematical structure required to address theoretical questions reqarding optimality. A second issue, which has many propsed solutions, is that DE's were not originally design to handle constrainted optimization, and so penalty methods typically are used. While penalty functions can provide feasible results, their weighting parameters require trial and error to avoid over or underpenalizing infeasible solutions, which can lead to a distortion of the search space. Other methods have been suggested,[16] however in the present work, penalty functions have been selected. DE's are stochastic algorithms and their convergence is defined as a convergence in the probability of the algorithm.[13] This means assuming an optimal solution exists with a probability of one, to ensure that the final solution is the optimal one, an infinite number of runs must be performed. For this reason, solutions obtained using genetic or evolutionary algorithms should be first considered as suboptimal unless proven otherwise. In the present

DOI: 10.13009/EUCASS2019-1038

study, each target trajectory was obtained after peforming 10 runs of the DE algorithm. The objective function in the DE algorithm is defined as,

$$\tilde{J}_1 = \sum_{i=1}^{N} \Delta V_i + p_r \|\delta\vec{r}\| + p_v \|\delta\vec{v}\| + p_m \frac{\delta m_{arr}}{m_0} \quad , \tag{20}$$

where N is the number of nodes used in the transcription procedure, presently set to 30, p_r, p_v, p_m are the weighting parameters, and $\delta\vec{r}$, $\delta\vec{v}$ and δm_{arr} are the matchpoint errors between forward and backward propagation of position, velocity and mass used in Sims-Flanagan (SF) transcription.[21] The variables m_{arr}, m_0 are the arrival and intial spacecraft masses, respectively, and all terms are normalized by appropriate factors to set the penalty in units of [au]. Unlike the original approach, the addition of the last term in Eqn. (20) is added in the present work to further force continuity in the mass at the matchpoint.

SF transcription is a method to approximate continuous low-thrust maneuvers and has been widely used in the space community, so only a brief description is provided. In the SF approach, the trajectory is approximated as a series N Keplerian propagation arcs, where at the center of each arc a node is placed, where a ΔV_i impulse is executed. Each ΔV_i is computed as,

$$\Delta V_i = \frac{\tau_i s_i T_{max} t_m}{m_i N} \quad , \tag{21}$$

where τ_i is the throttle level in the interval [0,1], T_{max} the maximum thrust level of 1.5 mN, m_i the instantaneous spacecraft mass, t_m, the time of flight of the interplanetary trajectory, and s_i is the toggle, lying in the set {0,1}, indicating the thruster is off or on, respectively. The low-thrust trajectory is then approximated by a series of Kepler arcs with impulses at each arc center. While providing an intial estimate, a real mission would require a transformation of the approximated trajectory to a real low-thrust trajectory. The Kepler arcs are propagated both forwards and backwards halfway up to the center matchpoint, where position, velocity and mass errors ($\delta\vec{r}$, $\delta\vec{v}$, δm) are driven to zero. After a solution is obtained from the global optimizer, local optimization is performed using *fmincon* in Matlab, where the initial guess is the solution obtained from DE. This allows the $m_{arr}, \delta\vec{r}, \delta\vec{v}$ to be further reduced up to a specified tolerance. Presently, the optimality and constraint tolerance are set to $1e^{-4}$ and $1e^{-5}$ and the position and velocity weighting parameters are set to 1000. The population size is set to 100 and the number of generations for each run was set to 2000, which resulted in a converged population profile. The number of trials of the DE for each trajectory (target) was 10, which did not correspond to a globally converged solution, however suboptimality may be claimed. To observe a trend towards global convergence a minimum of 100 to 200 trial should be performed, and for the present mission concept of multiple asteroid missions the computational requirements grow rapidly, and thus suboptimality was deemed sufficient. The objective function for the local optimizer is,

$$J_1 = \sum_{i=1}^{i=n} -m_{arr,i}, \tag{22}$$

where n is the number of cubeSats used in the mission. Due to the construction of patching both escape and interplanetary trajectories, in both the DE and local optimizer, $\tilde{J}_1, J_1$ are also subject to the constraint,

$$\|\vec{V}_{\infty,i}\| = \|\vec{V}_{ECI}(\tilde{t}_{0,i})\| \quad . \tag{23}$$

In Eqn. (23), $\vec{V}_{ECI}(\tilde{t}_{0,i})$ is simply the SOI velocity in the Earth-centered intertial frame and $\vec{V}_{\infty,i}$ is the excess velocity for the start of the interplanetary trajectory.

4.1 Target Selection

To select candidate targets for testing the proposed mission concept, potential targets were selected from the Global Trajectory Optimization Competition (GTOC) list of targets.[6] This list was selected due to its large database and it's suitability for the purpose of testing the mission concept, without focusing on the details of the asteroids. From this first list a cutoff filter was used to obtain a reduced list of targets with lower inclinations, eccentricities and semi-major axis, which is typically a requirement for near-Earth asteroid missions, particulary for miniature spacecraft. The cutoff criteria are,

$$\tilde{f} = \begin{cases} 0 & < i < 7 \\ 1 & < a < 1.4 \\ 0 & < e < 0.3 \end{cases} \quad . \tag{24}$$

Target selection algorithms can vary depending on the mission objectives, however typically targets are ranked by propellant required.[14] Due to the initial cutoff criteria in the first phase of target selection, all final targets produce

DOI: 10.13009/EUCASS2019-1038

propellant consumption within achievable limits for the interplanetary phase. The primary criteria in determining the final set of n targets depends on the propellant required for the ΔV_{corr} maneuver which requires considerable propellant compared to the deep space low-thrust trajectory. Once the final set of n candidates are selected based on total propellant requirements, $m_{corr} + m_p$, the deployment sequence is selected in order to parallelize the individual missions according to the objective,

$$J_2 = \sum_{i=1}^{n-1} \Delta t_0^i \tag{25}$$

$$= \sum_{i=1}^{n-1} (t_0^{j+1} - t_0^j) \quad . \tag{26}$$

subject to,

$$(t_0^{j+1} - t_0^j) < \Delta t_0^{max} \quad . \tag{27}$$

where Δt_0^{max} is set to 150 days. The number of cubeSats used to demonstrate the mission concept was selected as 5, from a final list of 22 feasible targets. It is noted that increasing the number of cubeSats deployed, n, reduces the parallelization due to a wider range of optimal deployment dates. As discussed in Section 2, the varying ISS orbital state must be taken into consideration when trying to obtain real-time solutions. To simplify the analysis in the present study a nominal reference date has been selected as demonstrated in Sections 2,3. Using a nominal reference date of May 15, 2019, feasible targets are selected, whose ΔV_{corr} have propellant requirements below 3.5 kg of propellant for the Hydros thruster. The variation in propellant requirements reflect one of many scenarios that could be encountered should the SOI velocity from the Earth escape maneuver be computed using the true of date ISS orbital parameters. Here the true of date refers to $\tilde{t}_{i,0} - t_{esc}$. In reality communications with ground networks will require realtime analysis of propellant requirements for ΔV_{corr} using predictive models. Once the cutoff filter, $\tilde{f}$ has been applied, the remaining target trajectories are placed in a sequence according to ascending epoch date, $\tilde{t}_{0,i}$. This results in a finite set of possible sequences;

$$|S| = N_0 - n + 1 \quad , \tag{28}$$

where N_0 is the set of all targets after feasibility using ΔV_{corr} has been checked, and minimal propellant trajectory selected for multiple trajectories for a single target. Note this set is a set of distinct target trajectories, orderd by ascending epoch. Additionally, if $n > N_0$ then n is set to N_0. The final sequence is the one which obtains the minimal J_2 value. The target selection procedure may be described as, $\tilde{f} \rightarrow \Delta V_{corr} < \Delta V_{corr,max} \rightarrow$ *for multiple feasible solutions for a single target, select one with minimal* m_p. This produces the set of N_0 candidates. Minimizing J_2 for all sequences in S, results in the final sequence.

Some discussion is provided here in regards to dealing with realtime ISS conditions. When considering the varying ISS orbital state, the primary concern is the affect of the orbital Ω and ω on the direction of the SOI velocity, which directly affects the propellant required for ΔV_{corr}. Figures 5a-5c demonstrate how variation in ISS orbital parameters affects the relative velocity escape vector, over a period of approximately one year. It may be observed from all figures that the variation within one year is roughly periodic. The variation presented in this data reflects primarily the perturbations encountered in the Earth system, however statistically at least once a year the ISS makes unpredicatable corrective maneuvers to avoid orbital collisions, for instance. While predictive models may capture the majority of ISS orbital states in the near future, models to capture unpredictive orbital corrections are less easily demonstrated, and perhaps only statistical or stochastic methods may approximate this behaviour for the short future time periods required to predict the SOI velocity for optimal deployment dates. In Figure 5(b), the line indicates the maximum tolerable propellant consumption for ΔV_{corr}. It can be seen that for roughly 50% of the time the ISS orbital state injects the cubeSat in a state that produces an SOI velocity that requires a ΔV_{corr} too large to be achievable by the proposed thruster. This shows the significance for good predictive models for ISS perturbations that can better approximate the propellant required for the maneuver. To construct missions that agree with the true ISS orbital states in the future, an excess amount of propellant for the ΔV_{corr} maneuver may be carried on board and ground communications on the date of deployment may be able to compute the difference between the ΔV_{corr} computed using models and the true ΔV_{corr} computed from the ISS orbital state on the date of deployment. Alternatively future propulsion technology may become further developed to ensure that throughout an entire period of an ISS orbital state, propellant requirements remain low enough to fit within cubeSat mass constraints.

5. Results

The results presented in this section have taken into consideration all major and necessary cubeSat components required for scientific observation missions of near-Earth asteroids. To ensure the initial mass of the 6U cubeSat, set to

DOI: 10.13009/EUCASS2019-1038

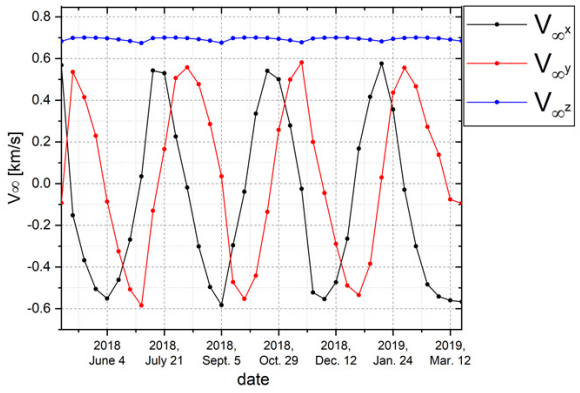

(a) Variation of $\vec{V}_\infty$ with variation of ISS orbital parameters for year between April 1, 2018 and April 1, 2019

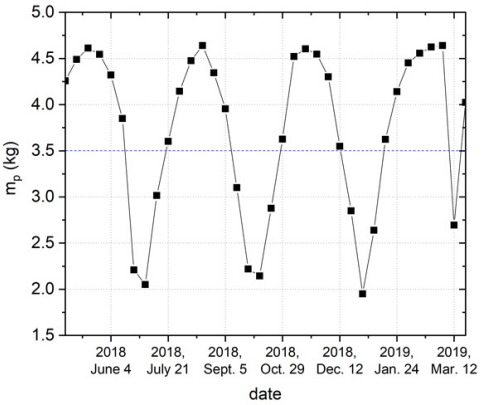

(b) Feasible target, ID 32 : variation of propellant required for ΔV_{corr} for range of ISS orbital parameters.

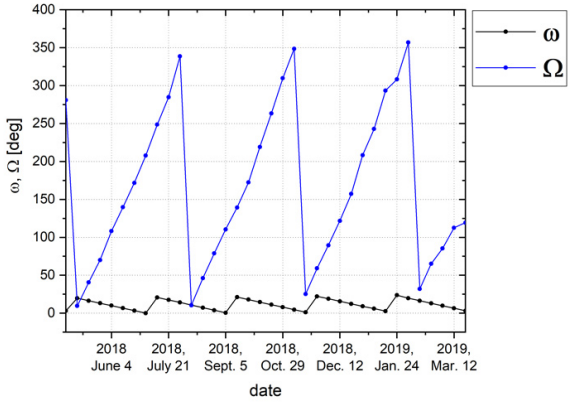

(c) Variation of ISS Ω, ω for year between April 1, 2018 and April 1, 2019

Figure 5: Target selection criteria and ISS orbital state variation. ISS orbital data provided by.[7]

12 kg (Table 1), could support a scientific interplanetary mission, off-the-shelf components were used to provide an approximate architecture. This architecture includes a a Blue Canyon XB6 Bus (which includes all components except for the payload),[3] a payload consisting of a deep space transponder, the ECAM M-50 Imager (Malin SSS),[25] 2 MiXi JPL thrusters, the Tethers Unlimited Hydros thruster, shielding and antennas. This allows a remaining 8 kg of mass available for propellant. To address safety concerns, cubeSat chemical thrusters using hydrazine were not considered and a water based propellant thruster was selected as discussed in Section 3.4. Table 1 presents the key spacecraft state parameters at time of deployment (initial state), during escape and end of escape/beginning of the interplanetary trajectory. While the escape time is relatively long in comparison to a cubeSat injected into a ballistic trajectory from a dedicated launch vehicle, the mission time, t_m, still remains below 1 year. The battery and solar cell degradation correspond to 27% and 11%, respectively, where solar cell degradation is not severe as may be expected for a mission duration of 300 days, possibly due to an escape orbital plane inclination of 51.6°, greatly reducing the intensity of the radiation dosage.

Still however, the time spent in the radiation belt is a concern, and it is not entirely known whether a 6U cubeSat could survive the escape trajectory in a state ready for a successfully interplanetary scientific mission. As small satellite technology continues to improve, the significant of these results show the feasibility from a systems perspective, of an entirely stand-alone cubeSat mission conducting its own scientific mission. Table 1 also indicates that the number of revolutions required for escape is 1383, which is reasonable given a starting altitude of 400 km. The Xenon propellant required by the low-thrust propulsion system is 2.53 kg for the entire maneuver, leaving a maximum of 2.5 kg of Xe propellant for the interplanetary mission when taking into account the propellant required for the ΔV_{corr} maneuver. The required propellant, m_p reported in Table 1 for the interplanetary mission includes both the mass for the low-thrust trajectory and the mass required for ΔV_{corr}.

DOI: 10.13009/EUCASS2019-1038

	deployment	escape	interplanetary
m_0 [kg]	12	—	9.47
P_{solar} [W]	125	112. 48	112.48
E_{batt} [Whr]	172	125.13	125.13
i [deg]	51.6	51.6	51.6
e	0.00011	(0-0.91)	elliptic
revolutions	—	1383	(0,2)
v_0 [km/s]	7.66	—	31.09
t_m [days]	—	300	[207, 1100]
m_p [kg]	—	2.53	[2.76, 3.46]

Table 1: Satellite state parameters at time of deployment, end of escape and duration of interplanetary trajectory.

target ID	target name	t_0	Δt [days]	m_{corr} [kg]	$m_{p,i}$ [kg]	t_m [days]	ΔV [km/s]
33	2006UQ216	17/10/2021	—	3.33	0	207.22	1.1
37	2007YT56	28/10/2021	11.25	3.08	0.38	742.25	2.22
30	2006KV89	26/11/2021	29.22	2.5	0.53	253.9	2.51
9	2000TE2	4/1/2022	39.07	2.74	0.02	1100	0.93
31	2006QV89	4/5/2022	119.9	3.23	0.13	489.65	1.48

Table 2: Selected targets and mission parameters based on target selection scheme.

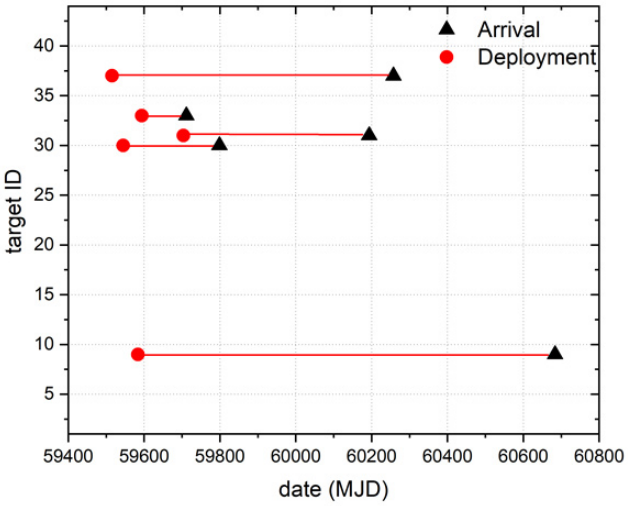

Figure 6: CubeSat missions time of flight overlap.

Table 2 shows the results of the interplanetary mission. The sequence is obtained using the algorithm described in Section 4.1. It is observed that the low thrust propellant requirements, $m_{p,i}$ are quite low, which is a primary reason for the feasibility of the mission concept due to larger requirements for ΔV_{corr}. One reason for this may be that constraining the initial interplanetary velocity using the patched conics method, reduces the initial orbital energy of the spacecraft, thus driving (sub)optimal trajectory results to longer times with lower ΔV. Typically to produce shorter mission times, the ΔV increases by factors of 1 km/s, increasing propellant requirements to $\sim$ 2 kg, where optimal values of V_∞ are closer to 3 km/s. Presently the SOI constraint fixed this value to 0.895 km/s, resulting in lower ΔV missions, thereby conserving propellant. While this does increase overall mission time, the scientific return is multiplied by a factor of n. The ΔV reported in Table 2, is the overall mission ΔV which includes both the interplanetary ΔV and the ΔV_{corr}. In Table 2, m_{corr} is the propellant required for ΔV_{corr}. This maneuver requires propellant masses between 2.5 and 3.3kg, producing the majority of propellant needs for the mission. Table 2 also demonstrates the extent to which the missions are parallelized. The greatest time between deployments is between targets 9 and 31, corresponding to 119 days, where

DOI: 10.13009/EUCASS2019-1038

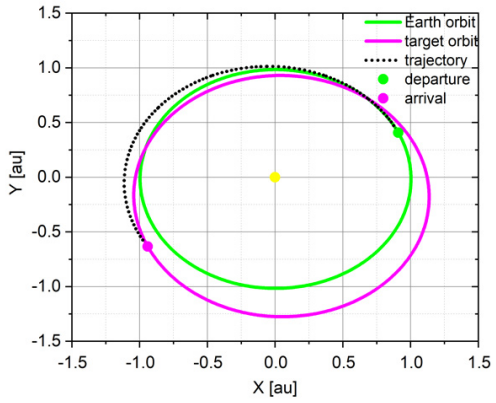

(a) Target 33 : a, e, i : 1.1 au, 0.16, 0.47 °

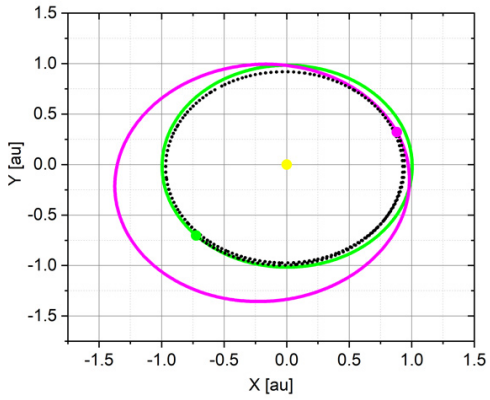

(b) Target 31 : a, e, i : 1.19 au, 0.22, 1.07 °

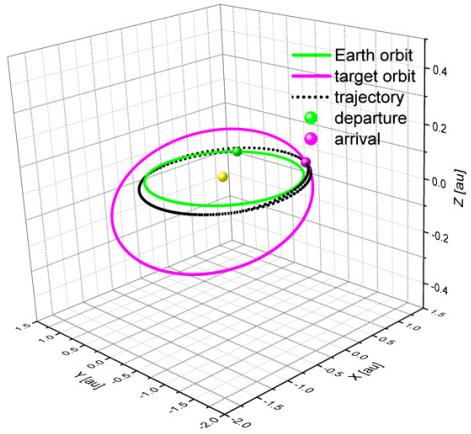

(c) Target 37 : a, e, i : 1.29, 0.29, 6 °

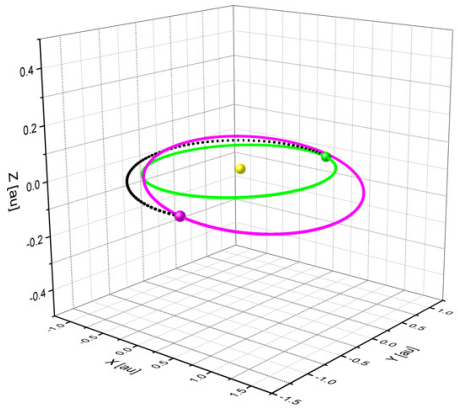

(d) Target 30 : a, e, i : 1.15 au, 0.27, 3.55 °

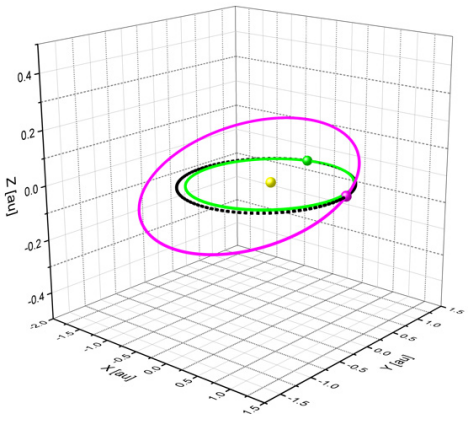

(e) Target 9 : a, e, i : 1.32 au, 0.21,6.22 °

Figure 7: Target trajectories optimized using DE and *fmincon* in Matlab.

the minimum Δt is 11 days. Figure 6 shows how well the missions overlap (in modified Julian days (MJD) vs target ID), where greater overlap is more desired. Target 9 produced the longest mission time, where its target asteroid has the greatest orbital inclination, making a direct transfer more difficult. In this case nearly 2 revolutions are required by the cubeSat to reach the target. Figure 6 shows that nearly all (sub)missions take place during the time it takes to complete the mission to target 9, showing nearly complete parallelization. Figure 7 demonstrate the trajectories in both $\mathbb{R}^2$ for lower inclination targets, and $\mathbb{R}^3$ for higher inclination targets. Here $\mathbb{R}^2$ corresponds to the projection in

DOI: 10.13009/EUCASS2019-1038

the xy (equatorial) plane. The trajectory for targets 33 and 30 produce direct transfers (less than a single revolution around the sun required), where the trajectory for target 9 requires nearly 2 revolutions. The trajectory for target 31 crosses slightly into Earth's orbit, which is typically avoided in trajectory design, however this can be corrected with an insertion in the trajectory optimization routine, and shouldn't impact results in any significant manner. While the scientific equipment is limited due to the mass constraints of a 6U cubeSat, the mission may be designed to reduced the number of cubeSats, to for instance to $n = 2$ or $n = 3$, while increasing the cubeSat form factor to 12U or 27U, allowing for a greater range of scientific payload.

6. Conclusions

This paper has presented a new framework for the parallel mission design of cubeSats to NEA, whose deployment strategy shows the potential for economic science class missions. Its feasibility was assessed through a detailed systems analysis for the escape duration of the mission, where trajectory patching techniques were demonstrated to connect the escape and interplanetary trajectories. Results were demonstrated for the parallelization of 5 cubeSats sent to distinct NEA targets, where the entire mission was nearly executed in parallel. The interplanetary trajectory was able to achieve low-propellant (sub)optimal solutions due to a reduced orbital energy at the start of the interplanetary trajectory. This increased the mission time both for individual cubeSat missions and the overall mission time taken from deployment of the first cubeSat to the arrival of the last cubeSat. This increased mission time is compensated by an increased scientific return factor achieved by deploying multiple small satellites. The advantage of multiple cubeSat deployment allows freedom to vary the objective for each individual mission to whatever is scientifically desired. CubeSats are still highly mass and volume constrained, which limits the amount of scientific payload, however the number of cubeSats deployed may be reduced should the cubeSat size be increased to accomodate more sophisticated scientific hardware. One challenge to consider when deploying from the ISS are the technical limitations in terms of trajectory design, and the requirement of strong predictive models for the ISS orbital states.The results presented here are significant for exploiting the potential of small satellites for deep space science missions, particulary as small satellite technology continues to improve. Future work is underway to optimize individual NEA cubeSat missions according to a detailed scientific return and to integrate an attitude control system alongside the global optimization scheme for increased trajectory and systems modelling accuracy.

7. Acknowledgments

The authors acknowledges the Warsaw University of Technology for financial support in conducting this research.

References

[1] AIAA. Guide to Modeling Earth's Trapped Radiation Enviornment. Number G-083-1999. American Institute of Astronautics and Aeronautics, Reston, VA, 1999.

[2] Richard.H. Battin. *An Introduction to the Mathematics and Methods of Astrodynamics*. American Institute of Aeronautics and Astronautics, Inc., 1999.

[3] BCT. XB6 Spacecraft (technical specifications). Blue Canyon Technologies, 2019. https://bluecanyontech.com/static/datasheet/BCT_DataSheet_Spacecraft_XB6.pdf.

[4] R.W. Conversano and R.E. Wirz. Mission Capability Assessment of Cubesats Using a Miniature Ion Thruster. *Journal of Spacecraft and Rockets*, 50(5), 2013.

[5] Stephen Creech. Nasa's Space Launch System: A Capability for Deep Space Exploration. NASA, 2014. Space Launch System (SLS) Program.

[6] ESA. GTOC4:Asteroid Billiard. Global Trajectory Optimization Competition Portal, 2009. https://sophia.estec.esa.int/gtoc_portal/?page_id=23.

[7] Dominic Ford. in-the-sky.org, 2019. Accessed February 2019 - May 2019.

[8] M.N. Ismail, A. Bakery, H.H. Selim, and M.H. Shehata. Eclipse intervals for satellites in circular orbit under the effects of earth's oblateness and solar radiation pressure. *NRIAG Journal of Astronomy and Geophysics*, 4:117–122, 2015.

DOI: 10.13009/EUCASS2019-1038

[9] JAXA. JEM Payload Accomadation Handbook- vol.8 - Small Satellite Deployment Interface Control Document. Japanese Aerospace Exploration Agency, 2015. JX-ESPC-101133-B.

[10] JAXA. Asteroid Explorer "Hayabusa2". Japanese Aerospace Exploration Agency, 2019. http://global.jaxa.jp/projects/sas/hayabusa2/topics.html.

[11] D. Korsmeyer. Cubesats and science return. NASA, 2015. The National Academies' Meeting on Achieving Science Goals with CubeSats, Washington, DC.

[12] Kristina Lemmer. Propulsion for Cubesats. *Acta Astronautica*, 134:231–243, 2017.

[13] M. Locatelli and M. Vasile. (non) convergence results for the differential evolution method. *Optimization Letters*, 9(3):413–425, 2014.

[14] A. Mereta and D. Izzo. Target Selection for a Small Low-thrust Mission to Near-Earth Asteroids. *Astrodynamics*, 2(3):249–263, 2018.

[15] S.R. Messenger, G.P. Summers, E.A. Burke, R.J. Walters, and M.A. Xapsos. Modeling Solar Cell Degradation in Space: A Comparison of the NRL Displacement Damage Dose and the JPL Equivalent Fluence Approaches. *Progress in Photovoltaics Research and Applications*, 9:103–121, 2001.

[16] M. Mezura-Montes, J. Reyes-Velazquez, and C.A. Coello. Modified Differential Evolution for Constrained Optimization. In *IEEE International Conference on Evolutionary Computation*, Vanvouver, Canada, July 2006.

[17] NASA. Small Spacecraft Technology State of the Art. Number TP-2015-216648/REV1. Mission Design Division, Ames Research Center, California, 2015.

[18] NASA. Mars insight landing press kit. National Aeronautics and Space Administration, 2018. (www.nasa.gov).

[19] Beny Neta and David Vallado. On Satellite Umbra/Penumbra Entry and Exit Positions. Number Version 1.50.001. Air Force Research Laboratory, 2017.

[20] Christopher Roth. IRENE:AE9/AP9/SPM/ Radiation Enviornment Model. Number NPS-MA-97-001. Naval Postgraduate School, Monterey, California, 1997.

[21] J.A. Sims and S.N. Flanagan. Preliminary Design of Low-Thrust Interplanetary Missions. *Advances in the Astronautical Sciences*, 103:583–592, 1999.

[22] S. Spangelo and B. Longmier. Optimization of Cubesat System-Level Design and Propulsion for Earth-Escape Missions. *Journal of Spacecraft and Rockets*, 52(4), August 2015.

[23] B. Stiltner. Cold Gas RCS for the NEA Scout Cubesat. National Aeronautics and Space Administration, October 2017. Report ID : 20170012396.

[24] R. Storn and K. Price. Differential Evolution - a Simple and Efficient Heuristic for Global Optimization over Continouos Spaces. *Journal for Global Optimization*, 11(4):341–359, December 1997.

[25] Malin Space Science Systems. Malin Space Science Systems, Exploration Through Imaging (ECAM-C50). Malin SSS, 2019. http://www.msss.com/brochures/c50.pdf.

[26] D.A. Vallado. *Fundamentals of Astrodynamics and Applications*. McGraw-Hill, 1997. US Dept. of Defense.

[27] M. Vavrina and K. Howell. Global Low-Thrust Trajectory Optimization Through Hybridization of a Genetic Algorithm and Direct Method. In *AIAA/AAS Astrodynamics Specialist Conference and Exhibit*, volume 2, pages 249–263, 2008.

[28] R. Walker, D. Koschny, and C. Bramanti. M-ARGO : A stand-alone deep space cubesat system for low-cost science and exploration missions. International Planetary Probe Workshop Small Sat Short Course, 2018. European Space Agency.

[29] J. Wang, P. Liu, J. Hicks-Garner, E. Sherman, S. Souzkiazian, M. Verbrugge, H. Tataria, J. Musser, and P. Finamore. Cycle-life model for graphite-lifepo4 cells. *Journal of Power Sources*, 196:3942–3948, 2011.

[30] C.H. Yam, F. Biscani, and D. Izzo. Global Optimization of Low-Thrust Trajectories via Impulsive Delta-V Transcription. Number ACT-RPR-MAD. European Space Agency, 2009.